

IGRF-14 secular variation prediction from core-surface flow acceleration

Frederik Dahl Madsen^{1,2}, Ciarán D. Beggan², William J. Brown², Richard Holme³,
Jonas Bregnhøj Lauridsen⁴, and Kathryn A. Whaler¹

¹ School of GeoSciences, University of Edinburgh, Edinburgh, United Kingdom.

² British Geological Survey, Lyell Centre, Edinburgh, United Kingdom.

³ School of Environmental Sciences, University of Liverpool, Liverpool, United Kingdom.

⁴ DTU Space, Technical University of Denmark, Kongens Lyngby, Denmark

October, 2024

Abstract

We submit a candidate model for the geomagnetic secular variation (SV) for the period 2025.0–2030.0 for the 14th generation of the International Geomagnetic Reference Field (IGRF-14). Our SV prediction is based on the inferred periodic behaviour of core-surface flow acceleration. The reasoning for this is based on recent evidence for core waves, the existence of which justifies periodic behaviour of core-surface flow acceleration. We obtain a core-surface flow model, in terms of poloidal and toroidal flow coefficients, from spatial gradient of SV data from Swarm from 2014.33–2024.00, and obtain flow acceleration from the first time derivative of these coefficients. This is done without relying on numerical simulations for prior information or enforcing any flow geometry (such as quasi-geostrophy). We fit each acceleration coefficient with a sinusoidal function, which is used to extend the function until 2030. We then obtain the flow coefficients through integration, and from flow we calculate the average predicted SV over the five year period.

1 Data

We use spatial gradients of SV to model the advective core-surface flow. With the European Space Agency’s Swarm mission (Friis-Christensen et al., 2006), we are able to obtain the spatial gradient of the magnetic field from across- and along track differences of the satellite measurements, which are more sensitive to changes in the magnetic field and SV than the “traditional” vector product (Kotsiaros and Olsen, 2014). We produce 4-monthly mean spatial gradient tensor SV data and error estimates, at 300 approximately regularly spaced geomagnetic virtual observatories (GVOs) for the period 2014.33 – 2024.00, following the methodology of Hammer et al. (2022).

2 Methods

2.1 Flow modelling

The reduced induction equation, assuming negligible diffusion (e.g. Roberts and Scott, 1965), relates the core-surface flow, \mathbf{u}_H , to the advected radial geomagnetic field, B_r , as:

$$\dot{B}_r + \nabla_H \cdot (\mathbf{u}_H B_r) = 0, \quad (1)$$

where $\dot{B}_r = \frac{\partial B_r}{\partial t}$ is its time derivative, and $\nabla_H = \nabla - \hat{\mathbf{r}} \cdot \nabla$ only contains horizontal derivatives.

Making the assumption that the geomagnetic field at the core-mantle boundary (CMB) is of internal origin, we can consider \mathbf{B} as the gradient of a potential

field, V , outside of the source region:

$$\mathbf{B} = -\nabla V(r, \theta, \phi), \quad (2)$$

where r , θ , and ϕ are spherical polar coordinates radius, colatitude, and longitude, respectively. Representing this potential field in spherical harmonics gives:

$$V(r, \theta, \phi) = a \sum_{l=1}^{L_B} \sum_{m=0}^l \left(\frac{a}{r}\right)^{l+1} (g_l^m \cos m\phi + h_l^m \sin m\phi) P_l^m(\cos \theta) \quad (3)$$

where $P_l^m(\cos \theta)$ are Schmidt quasi-normalised associated Legendre polynomials of degree and order l and m , respectively, a is the reference radius (6371.2 km), and g and h are weights, known as Gauss coefficients. Due to the static and small-scale crustal magnetic field (e.g. Cain et al., 1989), we truncate the magnetic field to degree $L_B = 14$.

We decompose the core surface flow into its toroidal and poloidal parts, since the equation below is only valid for the flow at the top of the core (Roberts and Scott, 1965). We thus express \mathbf{u}_H as:

$$\mathbf{u}_H = \nabla \times (\mathcal{T}\mathbf{r}) + \nabla_H(\mathcal{S}\mathbf{r}) \quad (4)$$

where \mathcal{T} and \mathcal{S} are the toroidal and poloidal scalar potentials, respectively. Like V , the flow potentials can be represented in terms of spherical harmonics:

$$\mathcal{T}(\theta, \phi) = \sum_{l=1}^{L_u} \sum_{m=0}^l (t_l^{m^c} \cos m\phi + t_l^{m^s} \sin m\phi) P_l^m(\cos \theta) \quad (5)$$

$$\mathcal{S}(\theta, \phi) = \sum_{l=1}^{L_u} \sum_{m=0}^l (s_l^{m^c} \cos m\phi + s_l^{m^s} \sin m\phi) P_l^m(\cos \theta)$$

By truncating the velocity fields at degree L_u , it is assumed that the energy of the flow is constrained within the length-scale related to L_u . We truncate at $L_u = 14$.

Equations (1)–(5) can be manipulated to relate the Gauss coefficients to the toroidal and poloidal coefficients:

$$\dot{\mathbf{g}} = \mathbf{E}\mathbf{t} + \mathbf{G}\mathbf{s}, \quad (6)$$

where vectors $\dot{\mathbf{g}}$, \mathbf{t} , and \mathbf{s} respectively contain the SV Gauss, toroidal velocity, and poloidal velocity coefficients, and matrices \mathbf{E} and \mathbf{G} depend on the main field coefficients and the Elsasser and Gaunt integrals, respectively (Gibson and Roberts, 1969; Whaler, 1986; Beggan and Whaler, 2010). We can express the time derivative of Equation (2) as:

$$\dot{\mathbf{d}} = \mathbf{Y}\dot{\mathbf{g}} \quad (7)$$

where elements of \mathbf{Y} contain spherical harmonics and their derivatives, and $\dot{\mathbf{d}}$ is a vector containing the spatial gradients of SV. We can then link the SV data to the flow coefficients by substituting Equation (7) into Equation (6):

$$\dot{\mathbf{d}} = \mathbf{Y}\mathbf{E}\mathbf{t} + \mathbf{Y}\mathbf{G}\mathbf{s} \equiv \mathbf{A}\mathbf{m} \quad (8)$$

Here, \mathbf{A} is the normal equations matrix and \mathbf{m} is the model vector containing the toroidal and poloidal flow coefficients. Recognising the ill-determined nature of the problem (Holme, 2015), we employ a regularised least-squares solution (e.g. Whaler, 1986). We invert data from the 300 GVOs at multiple epochs simultaneously, regularising the solution both temporally and spatially (Whaler et al., 2016, 2022). We choose to regularise our model temporally in order to minimise the acceleration between epochs. For the spatial regularisation, we choose the ‘strong norm’, originally proposed by Bloxham (1988), which minimises the second spatial derivatives of the flow, averaged across the CMB, thus penalising spatial complexity:

$$\int_{\Omega} ((\nabla_H^2 u_{\theta})^2 + (\nabla_H^2 u_{\phi})^2) d\Omega, \quad (9)$$

where (u_{θ}, u_{ϕ}) are meridional and azimuthal flow components, respectively, and Ω is the surface of the CMB

The regularized least-squares solution to Equation (8) thus takes the form

$$\hat{\mathbf{m}} = (\mathbf{A}^T \mathbf{C}_e^{-1} \mathbf{A} + \lambda_v \mathbf{C}_m^{-1} + \lambda_t \mathbf{D}^T \mathbf{D})^{-1} \mathbf{A}^T \mathbf{C}_e^{-1} \dot{\mathbf{d}} \quad (10)$$

where, \mathbf{C}_e is the data covariance matrix, \mathbf{C}_m is the *a priori* model covariance matrix (implementing the strong norm), λ_v and λ_t are the spatial and temporal damping factors, respectively, and \mathbf{D}_j is the temporal first differences matrix (see Whaler et al., 2016). This model is developed by Madsen et al. (in prep., see Swarm 10th anniversary special issue).

From this flow model, we obtain core-surface flow acceleration by taking the discrete four-monthly time derivative for each flow coefficient as following:

$$\mathbf{a}_{t+\frac{1}{2}} = \frac{\mathbf{u}_{H,t+1} - \mathbf{u}_{H,t}}{\Delta t} \quad (11)$$

where t signifies the epoch of data, and $\Delta t = \frac{1}{3}$ years is the time between successive epochs.

2.2 Forecasting - fitting sinusoidal functions to core-surface flow acceleration

Given the high data-quality available from Swarm, we can now readily resolve core-surface flow acceleration. Results from Madsen et al. (in prep., see Swarm 10th anniversary special issue) and Grüne et al. (in prep., see Swarm 10th anniversary special issue) showed that the flow-acceleration coefficients vary around zero on intradecadal to decadal time-scales with some periodic tendencies.

To investigate periodic signals in the acceleration coefficients, we employ a similar method to Holme and de Viron (2013), and set up a simple inversion scheme to solve for the best fit amplitude and phase of a sinusoidal signal for each coefficient, using a least-squares approach. Considering the input signal as the vector γ of length N , we relate γ to a sinusoidal signal as a function of time t with period T , $s(t) = A \sin \frac{2\pi t}{T} + B \cos \frac{2\pi t}{T}$, through the relation

$$\gamma = \mathbf{X}\mathbf{p} \quad (12)$$

where the condition matrix \mathbf{X} contains the sinusoidal variations as a function of time, and the model vector \mathbf{p} contains the amplitudes, as

$$\mathbf{X}(t) = \begin{bmatrix} \sin \frac{2\pi t}{T} & \cos \frac{2\pi t}{T} \end{bmatrix}; \quad \mathbf{p} = \begin{bmatrix} A \\ B \end{bmatrix}$$

For any given period, we can thus calculate the best fit amplitudes by solving Equation 12 with a least-squares approach, yielding the best fit model vector $\hat{\mathbf{m}}$ to the data:

$$\hat{\mathbf{p}} = (\mathbf{X}^T \mathbf{X})^{-1} \mathbf{X}^T \gamma \quad (13)$$

$\hat{\mathbf{p}}$ is found from the best combination of A and B that yields the lowest least-square residual, ϵ , between true data γ and the modelled data $\hat{\gamma}$:

$$\epsilon = \sum_i^N (\gamma_i - \hat{\gamma}_i)^2 \quad (14)$$

This inversion is linear, but only if T is defined. To find the best fit period, we repeat this inversion with values of T between 1 and 20 years. We select the best suited period, based on the lowest ϵ value after the inversion is complete for each T for each acceleration coefficient. Given that we have 10 years of data, we allow for T to increase up to 20 years as a proxy for flow-acceleration coefficients that may appear to vary in a strictly linear fashion over the past 10 years.

To avoid interannual noise dominating the periodic signature of the acceleration coefficients, we fit each coefficient with a damped least-squared spline (Constable and Parker, 1988, e.g.) before iterating the inversion over values of T . After finding the best fit period for each flow-acceleration coefficient, we create a sinusoidal time-series from 2014.33–2030.00 with that period. We then integrate the coefficients to obtain flow velocity, using the velocity from our flow model obtained from Equation (10) at epoch 2014.33 as the integration constant. Finally, we obtain SV from our predicted flow, using Equation (6). We will refer to this model as our candidate model.

3 Results

The solid lines in Figure 1 show the acceleration coefficients obtained from our core-surface model, made using spatial gradients of SV from Swarm, shown up to degree and order 8. We see here that most coefficients, for example $\partial t_3^0 c / \partial t$ and $\partial s_3^0 c / \partial t$, show convincingly periodic behaviour during the Swarm era. Some coefficients, however, like $\partial s_4^0 c / \partial t$ appears to behave in a more linear manner.

Also shown in Figure 1, as insets, are the relative fits for different periods to each acceleration coefficient. This is calculated using Equation (14). We pick the best fit period where there is a clear peak in the curve. If there is no peak, we set $T = 20$. If there are two peaks, we pick the peak with the higher amplitude. Flow-acceleration coefficients for our candidate model are shown by the dotted lines in Figure 1, extended to 2030. We see that they manage to capture the overall trend of the coefficients, where coefficients vary around zero. However, a few coefficients like $\partial s_4^4 s / \partial t$ vary periodically at an offset from zero, and so the periodic fit is shifted from the observed acceleration.

Figure 2 shows annual snapshots of the predicted flow these acceleration coefficients. We get these by first rearranging Equation (11) for $\mathbf{u}_{\mathbf{H}t+1}$ to obtain our flow coefficients. For $\mathbf{u}_{\mathbf{H}t=0}$, we use the values for the first epoch of our initial flow model. We then calculate the core-surface flow using Equations (4) and (5). The flow shows a persistent eccentric planetary gyre (e.g. Pais and Jault, 2008), a strong westward jet underneath the Bering Strait (e.g. Livermore et al., 2017), and westward flow underneath the Atlantic ocean (e.g. Holme, 2015), consistent with other studies of core-surface flow. Under the Pacific ocean, our models show

a weak eastward flow in 2025 that increases in magnitude with time. The flow is superposed on the poloidal flow potential, \mathcal{S} , which shows the amount of up- and downwelling, where $\mathcal{S} > 0$ indicates upwelling. Although the flow is dominated by large-scale toroidal flow, primarily in the eccentric planetary gyre, our flow also shows interesting poloidal flow patterns, mostly centered around low latitudes. Most notable is the strong downwelling underneath the equatorial west Pacific, where the westwards Atlantic flow and eastwards Pacific flow collide. Our model predicts that this weakens and move southwards with time. We also see a strengthening region of upwelling underneath Southeast Asia. At high Northern latitudes, we also see strengthening up- and downwelling on either side of the core surface below the Bering Strait.

Finally, we obtain SV coefficients from the flow-model, using Equation (6). These are shown by dot-dashed lines in Figure 3, where SV coefficients from CHAOS-7.18 (Finlay et al., 2020, purple dotted lines) and the core-surface flow model (solid lines) are also shown for reference. We see that, for most of the SV coefficients, our model is in good agreement with the core-surface flow model and CHAOS. However, given that we only allowed for pure sinusoidal variation of flow-acceleration, the sinusoidal model predictions sometimes deviate from the ‘observed’ SV. An example of this is $\partial h_4^5 / \partial t$, where SV from CHAOS and the initial core-surface flow model decreases after 2020, but our candidate model increases.

We obtain our coefficients for submission by calculating the average value for each SV coefficients up to degree and order 8 in the time-period 2025–2030. Our final values are shown by the pluses in Figure 3, and are provided in Table 1. From these, we calculated SV components in geocentric coordinates, at the Earth’s surface. These are shown in Figure 4. Note we do not estimate any formal uncertainties associated with the Gauss coefficients.

4 Summary and Discussion

We see in Figure 3 that our candidate model is in good agreement with the input flow model and CHAOS-7.18 for the majority of the SV coefficients. The predicted SV after 2024 is variable, given the dynamic nature of our model. Our model thus allow for non-linear variations, such as geomagnetic jerks (e.g. Brown et al., 2013; Aubert et al., 2022). Although we note that

there is no understood link between variations in SV coefficients and geomagnetic jerks, we note that it is possible for our model to include jerks. Work is ongoing to determine whether our candidate model predicts any jerks in the period 2025–2030.

Figure 2 shows the predicted flow evolution. As noted in Section 3, our model predicts a weakening in the downwelling region in the east equatorial Pacific. Interestingly, our model predicts a strengthening of the upwelling underneath southeast Asia. This results in an increased flow velocity in the west equatorial Pacific, a region in which the 2017 and 2020 jerks appeared as a result of pulses in core-surface acceleration (Madsen et al., in prep.). Following on from the results of Ropp and Lesur (2023), who analysed the change in flow direction in the Pacific from west to eastwards, our model predicts that the eastward Pacific is accelerating. In comparison to the Pacific, our model predicts relatively little change underneath the Atlantic. This is in contrast to the 2000’s, where the flow underneath the Pacific was quasi-steady, and the Atlantic region saw more dynamic flow (e.g. Chulliat and Maus, 2014).

Our IGRF-14 candidate model is based on assumed periodic dynamics of core-surface flow. This is primarily inspired by the growing evidence for hydromagnetic waves propagating along the core-mantle boundary (e.g. Gillet et al., 2022; Istaş et al., 2023; Finlay et al., 2023; Gerick and Livermore, 2024). With the increased data-quality from satellite measurements, as well as quasi-continuous near-global sampling of the geomagnetic field from satellites over the past 26 years, we are now able to investigate intradecadal periodic variations in core-surface flow dynamics (Grüne et al., in prep.). As we show in Figure 1, we can reasonably fit individual time-varying flow-acceleration coefficients over the past 10 years with a sinusoidal function fixed for a single period. Figure 5 shows a histogram of the best fit periods for the toroidal and poloidal flow-acceleration coefficients. We see here that about half of the coefficients could be fitted with a period within the length of the time-series, and most coefficients can be fit with a period of 15 years or less.

We have presented a predictive model for SV calculated from a model of periodically varying flow acceleration. The flow velocity is given by the integral of this function, governed by an initial value, or equivalently an arbitrary constant — in our case, the values for the first epoch of our initial flow model. Such a near-constant flow yields a near-constant SV, consistent with

conventional modelling of the secular variation for field prediction, most specifically with the framework of the IGRF. Using the oscillatory model for variations in this flow has the additional benefit that if extended outside the region of the prediction, it will remain bounded, something not the case for other possible representations of more detailed temporal variation (polynomial or exponential variations). As a result, the time evolution of the model remains bounded. It may not be physically sufficient, or even correct, but at least it is not divergent, and so is part of the space of flows and resulting secular variation that are physically possible. The oscillatory nature is also consistent with the idea that intra- to bidecadal core-surface dynamics is dominated by periodic behaviour (e.g. [Gillet et al., 2022](#))

Table 1: IGRF-14 candidate SV coefficients for 2025–2030.

l	m	\dot{g}_l^m	\dot{h}_l^m
1	0	13.34	0.00
1	1	13.97	-20.79
2	0	-9.84	0.00
2	1	-5.89	-25.40
2	2	-3.16	-16.12
3	0	-1.27	0.00
3	1	-5.89	7.34
3	2	1.55	-0.29
3	3	-12.40	1.42
4	0	-0.78	0.00
4	1	-1.10	-1.42
4	2	-8.06	5.82
4	3	5.08	0.99
4	4	-5.19	-4.40
5	0	0.21	0.00
5	1	0.64	-0.34
5	2	-0.79	1.80
5	3	0.20	-1.93
5	4	2.16	3.62
5	5	2.41	1.44
6	0	-0.64	0.00
6	1	0.01	0.17
6	2	0.27	-1.94
6	3	1.27	-1.18
6	4	-1.20	0.55
6	5	0.18	1.56
6	6	1.18	0.41
7	0	0.17	0.00
7	1	-0.45	0.81
7	2	-0.10	0.47
7	3	0.89	-0.44
7	4	0.26	-0.24
7	5	-0.67	-0.90
7	6	-0.94	0.30
7	7	0.69	-0.24
8	0	-0.02	0.00
8	1	0.27	-0.23
8	2	-0.27	0.35
8	3	0.46	0.01
8	4	-0.02	0.65
8	5	0.28	-0.30
8	6	0.27	-0.25
8	7	-0.12	0.45
8	8	0.05	0.18

References

Aubert, J., Livermore, P. W., Finlay, C. C., Fournier, A., and Gillet, N. (2022). A taxonomy of simu-

- lated geomagnetic jerks. *Geophysical Journal International*, 231(1):650–672.
- Beggan, C. and Whaler, K. (2010). Forecasting secular variation using core flows. *Earth, Planets and Space*, 62(10):11.
- Bloxham, J. (1988). The determination of fluid flow at the core surface from geomagnetic observations. In Vlaar, N. J., Nolet, G., Wortel, M. J. R., and Cloetingh, S. A. P. L., editors, *Mathematical Geophysics: A Survey of Recent Developments in Seismology and Geodynamics*, pages 189–208. Springer Netherlands, Dordrecht.
- Brown, W. J., Mound, J. E., and Livermore, P. W. (2013). Jerks abound: An analysis of geomagnetic observatory data from 1957 to 2008. *Physics of the Earth and Planetary Interiors*, 223:62–76.
- Cain, J. C., Wang, Z., Schmitz, D. R., and Meyer, J. (1989). The geomagnetic spectrum for 1980 and core-crustal separation. *Geophysical Journal International*, 97(3):443–447.
- Chulliat, A. and Maus, S. (2014). Geomagnetic secular acceleration, jerks, and a localized standing wave at the core surface from 2000 to 2010. *Journal of Geophysical Research: Solid Earth*, 119(3):1531–1543.
- Constable, C. G. and Parker, R. L. (1988). Smoothing, splines and smoothing splines; Their application in geomagnetism. *Journal of Computational Physics*, 78(2):493–508.
- Finlay, C. C., Gillet, N., Aubert, J., Livermore, P. W., and Jault, D. (2023). Gyres, jets and waves in the Earth’s core. *Nature Reviews Earth & Environment*.
- Finlay, C. C., Kloss, C., Olsen, N., Hammer, M. D., Tøffner-Clausen, L., Grayver, A., and Kuvshinov, A. (2020). The CHAOS-7 geomagnetic field model and observed changes in the South Atlantic Anomaly. *Earth, Planets and Space*, 72(1):156.
- Friis-Christensen, E., Lühr, H., and Hulot, G. (2006). Swarm: A constellation to study the Earth’s magnetic field. *Earth, Planets and Space*, 58(4):351–358.
- Gerick, F. and Livermore, P. (2024). Interannual Magneto-Coriolis modes and their sensitivity on the magnetic field within the Earth’s core.
- Gibson, R. D. and Roberts, P. H. (1969). The Bullard-Gellman dynamo. In Runcorn, S. K., editor, *Applications of Modern Physics to the Earth and Planetary Interiors*, pages 577–602.
- Gillet, N., Gerick, F., Jault, D., Schwaiger, T., Aubert, J., and Istas, M. (2022). Satellite magnetic data reveal interannual waves in Earth’s core. *Proceedings of the National Academy of Sciences*, 119(13):e2115258119.
- Hammer, M. D., Finlay, C. C., and Olsen, N. (2022). Secular variation signals in magnetic field gradient tensor elements derived from satellite-based geomagnetic virtual observatories. *Geophysical Journal International*, 229(3):2096–2114.
- Holme, R. (2015). 8.04 - Large-Scale Flow in the Core. In Schubert, G., editor, *Treatise on Geophysics (Second Edition)*, pages 91–113. Elsevier, Oxford.
- Holme, R. and de Viron, O. (2013). Characterization and implications of intradecadal variations in length of day. *Nature*, 499(7457):202–204.
- Istas, M., Gillet, N., Finlay, C. C., Hammer, M. D., and Huder, L. (2023). Transient core surface dynamics from ground and satellite geomagnetic data. *Geophysical Journal International*, 233(3):1890–1915.
- Kotsiaros, S. and Olsen, N. (2014). End-to-End simulation study of a full magnetic gradiometry mission. *Geophysical Journal International*, 196(1):100–110.
- Livermore, P., Hollerbach, R., and Finlay, C. (2017). An accelerating high-latitude jet in Earth’s core. *Nature Geoscience*, 10(1):62–68.
- Pais, M. A. and Jault, D. (2008). Quasi-geostrophic flows responsible for the secular variation of the Earth’s magnetic field. *Geophysical Journal International*, 173(2):421–443.
- Roberts, P. H. and Scott, S. (1965). On Analysis of the Secular Variation — 1. A Hydromagnetic Constraint: Theory. *Journal of geomagnetism and geoelectricity*, 17(2):137–151.
- Ropp, G. and Lesur, V. (2023). Mid-latitude and equatorial core surface flow variations derived from observatory and satellite magnetic data. *Geophysical Journal International*, 234(2):1191–1204.

- Waler, K. A. (1986). Geomagnetic evidence for fluid upwelling at the core-mantle boundary. *Geophysical Journal of the Royal Astronomical Society*, 86(2):563–588.
- Waler, K. A., Hammer, M. D., Finlay, C. C., and Olsen, N. (2022). Core Surface Flow Changes Associated With the 2017 Pacific Geomagnetic Jerk. *Geophysical Research Letters*, 49(15):e2022GL098616.
- Waler, K. A., Olsen, N., and Finlay, C. C. (2016). Decadal variability in core surface flows deduced from geomagnetic observatory monthly means. *Geophysical Journal International*, 207(1):228–243.

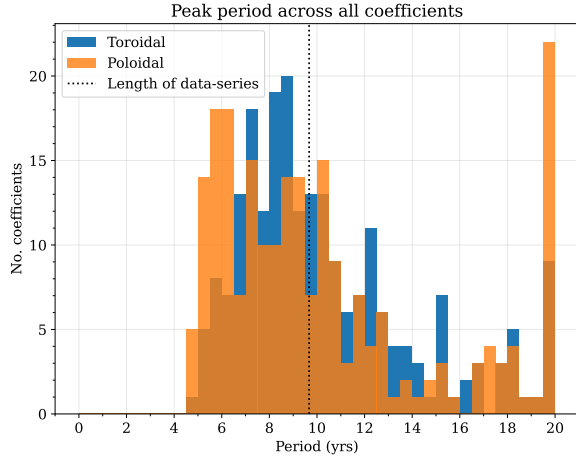


Figure 5: Histogram showing the distribution of best-fit periods for the poloidal (orange) and toroidal (blue) flow-acceleration coefficients up to degree 14. The black-dotted line marks the length of the flow-model. Coefficients with no clear periodicity has an imposed period of $T = 20$

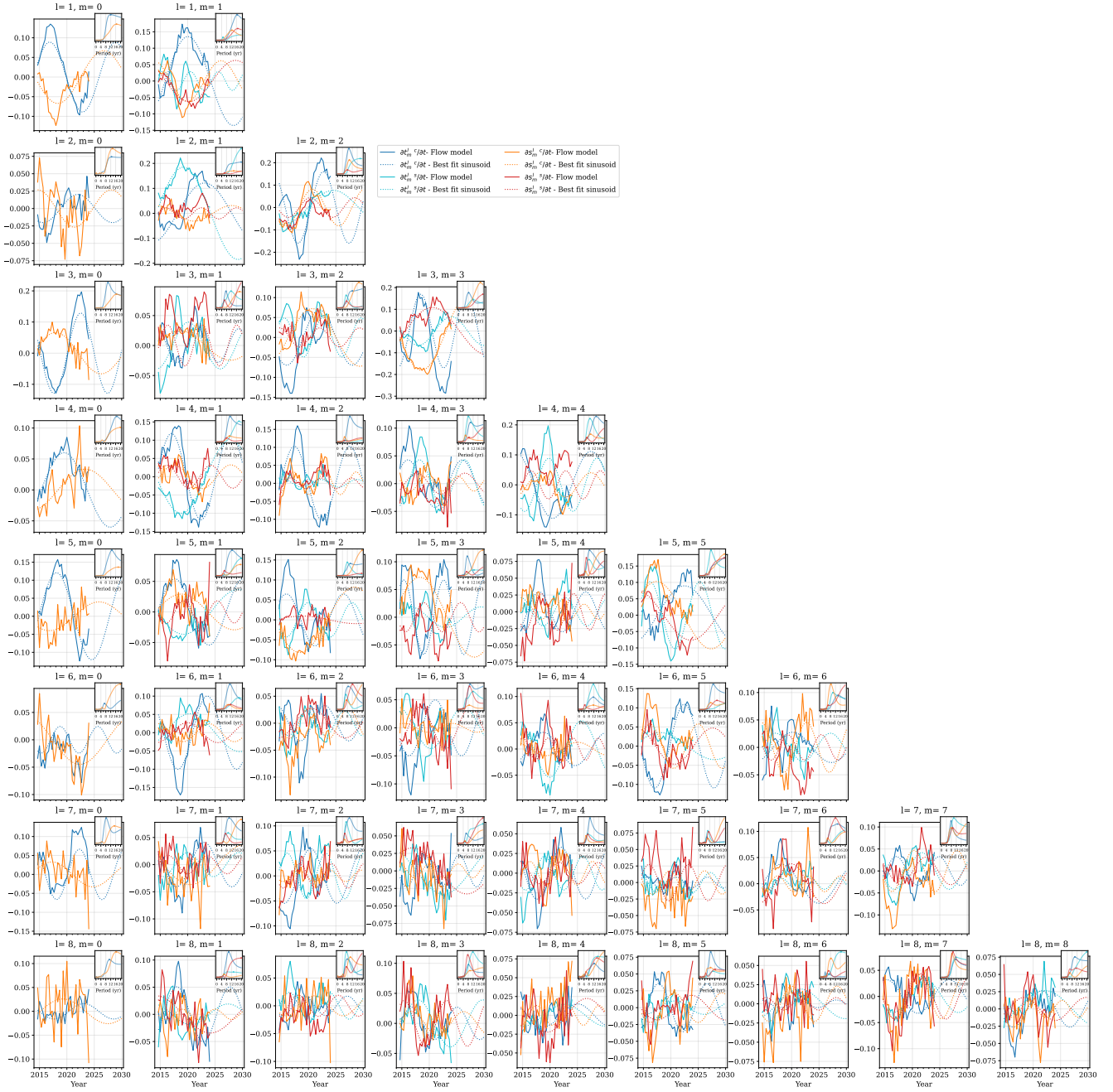


Figure 1: Toroidal (blue and turquoise) and poloidal (orange and red) flow-acceleration coefficients from 2014. Solid lines show flow acceleration from the core-surface flow model, and dotted lines show sinusoidal prediction. Rows show spherical harmonic degree, and columns spherical harmonic order. Insets show relative fit to data for sinusoidal functions as a function of period T . Dots show the chosen period. Note that the y-scale varies for each order and degree.

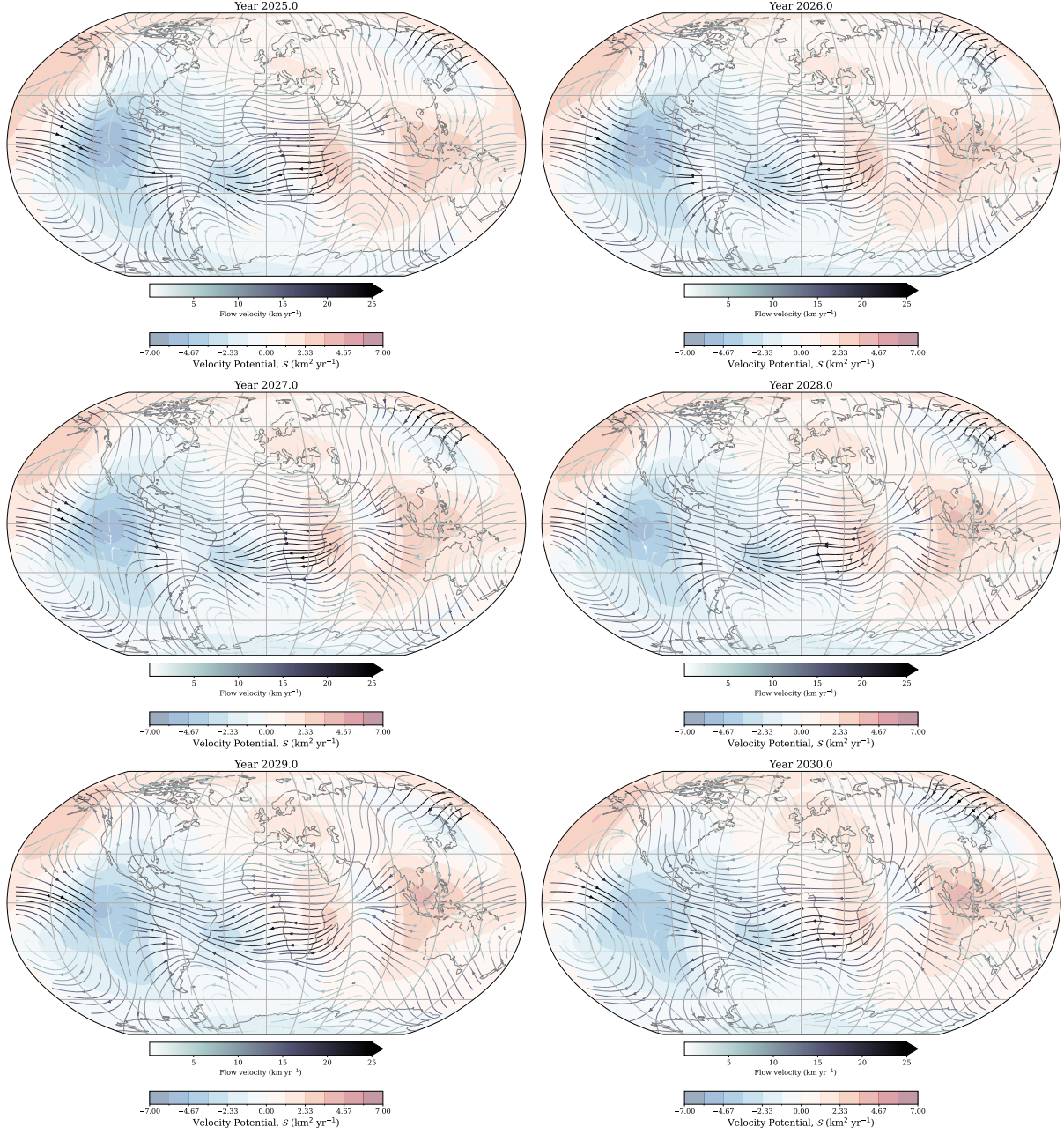


Figure 2: Snapshots of predicted flows from 2025.0 to 2030.0. Flow is superimposed on poloidal flow potential, S . Plots are in Robinson projection, and continents are shown for reference only.

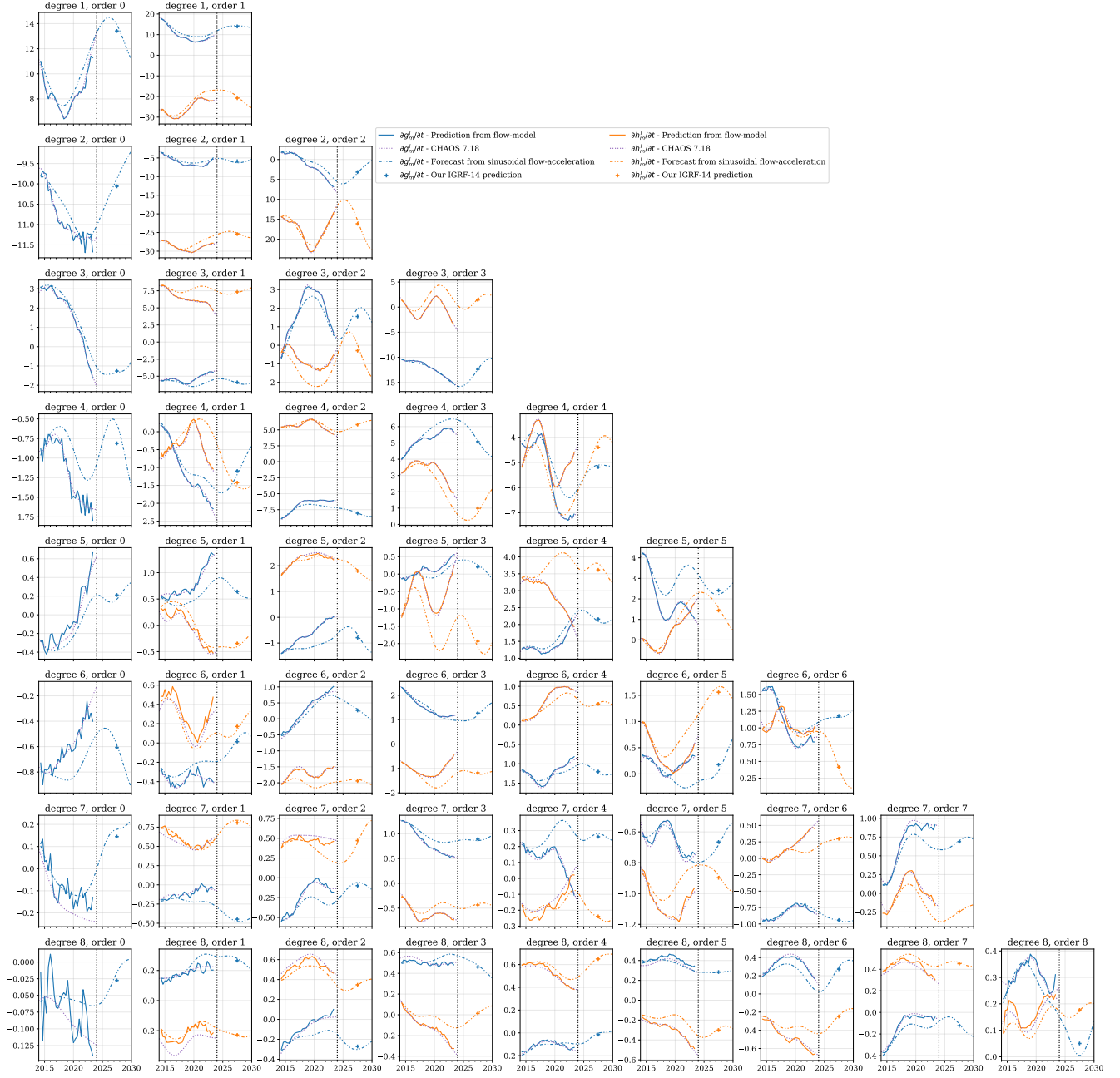


Figure 3: SV Gauss coefficients, g_l^m (blue) and h_l^m (orange), from 2014 to 2030. Solid lines are from the core-surface flow model, and dotted lines show predictions from our candidate model. The ‘+’ symbols marks our IGRF-14 SV predictions, centered at the year 2027.5. Purple line shows CHAOS-7.18 prediction for reference (Finlay et al., 2020). Rows show spherical harmonic degree, and columns spherical harmonic order. Note that the y-scale varies for each order and degree.

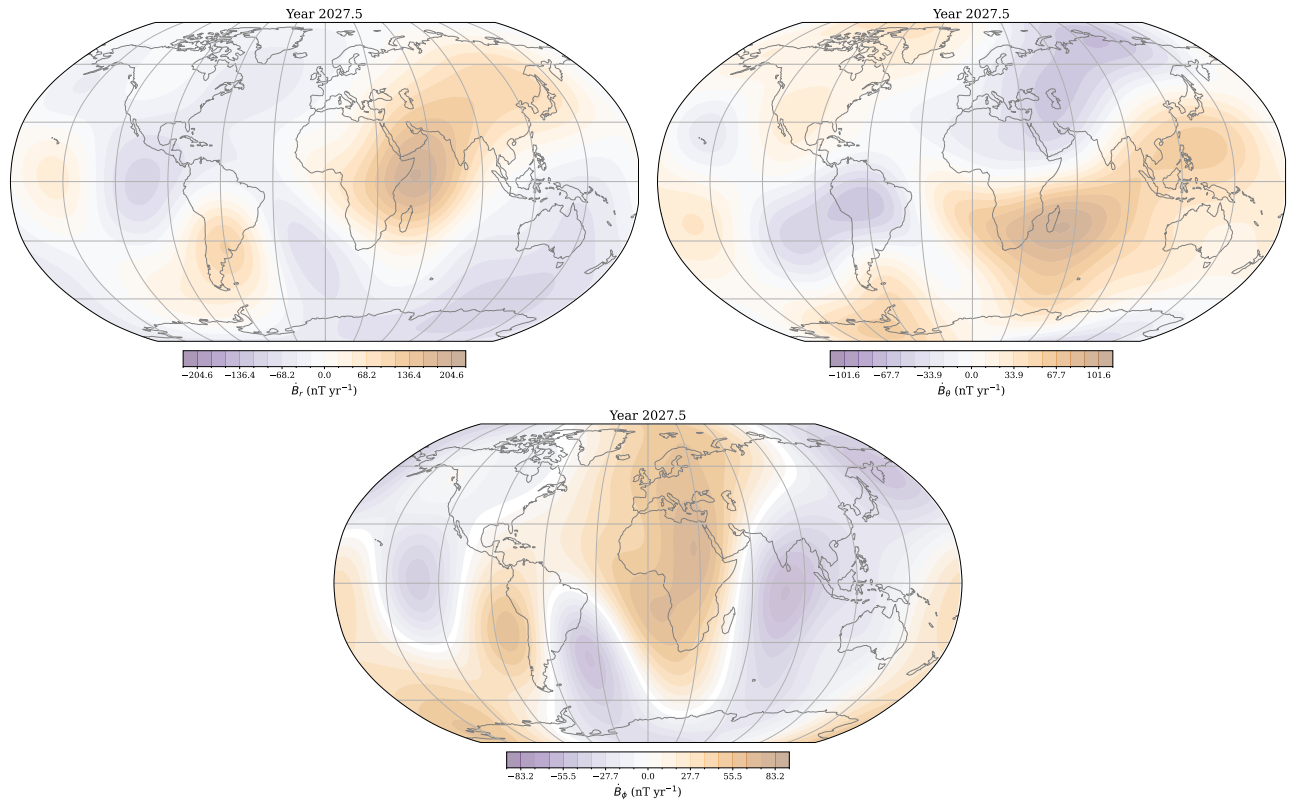


Figure 4: Radial (\dot{B}_r), meridional (\dot{B}_θ), and azimuthal (\dot{B}_ϕ) SV as predicted by our candidate model, in 2027.5. The SV is plotted at the IGRF reference Earth radius ($a = 6371.2$ km). Note that each plot has a different value range. Plots are in Robinson projection.